Electronic Supplementary Information (ESI)

Mesoporous $MnCo_2O_4$ with Abundant Oxygen Vacancy Defects as High-Performance Oxygen Reduction Catalysts

Tian Yi Ma, Yao Zheng, Sheng Dai, Mietek Jaroniec and Shi Zhang Qiao**

Dr. T. Y. Ma, Y. Zheng, A/Prof. S. Dai, Prof. S. Z. Qiao,
School of Chemical Engineering, The University of Adelaide,
Adelaide, SA 5005, Australia
E-mail: s.qiao@adelaide.edu.au; s.dai@adelaide.edu.au

Prof. M. Jaroniec
Department of Chemistry and Biochemistry, Kent State University,
Kent, Ohio 44240, USA

Table S1 Elemental analysis of m-$MnCo_2O_4$ and b-$MnCo_2O_4$.

Sample	Mn (wt.%)	Co (wt.%)	O (wt.%)	Formula
m-$MnCo_2O_4$	23.59	50.63	25.78	$MnCo_2O_{3.75}$
b-$MnCo_2O_4$	23.23	49.84	26.93	$MnCo_2O_{3.98}$

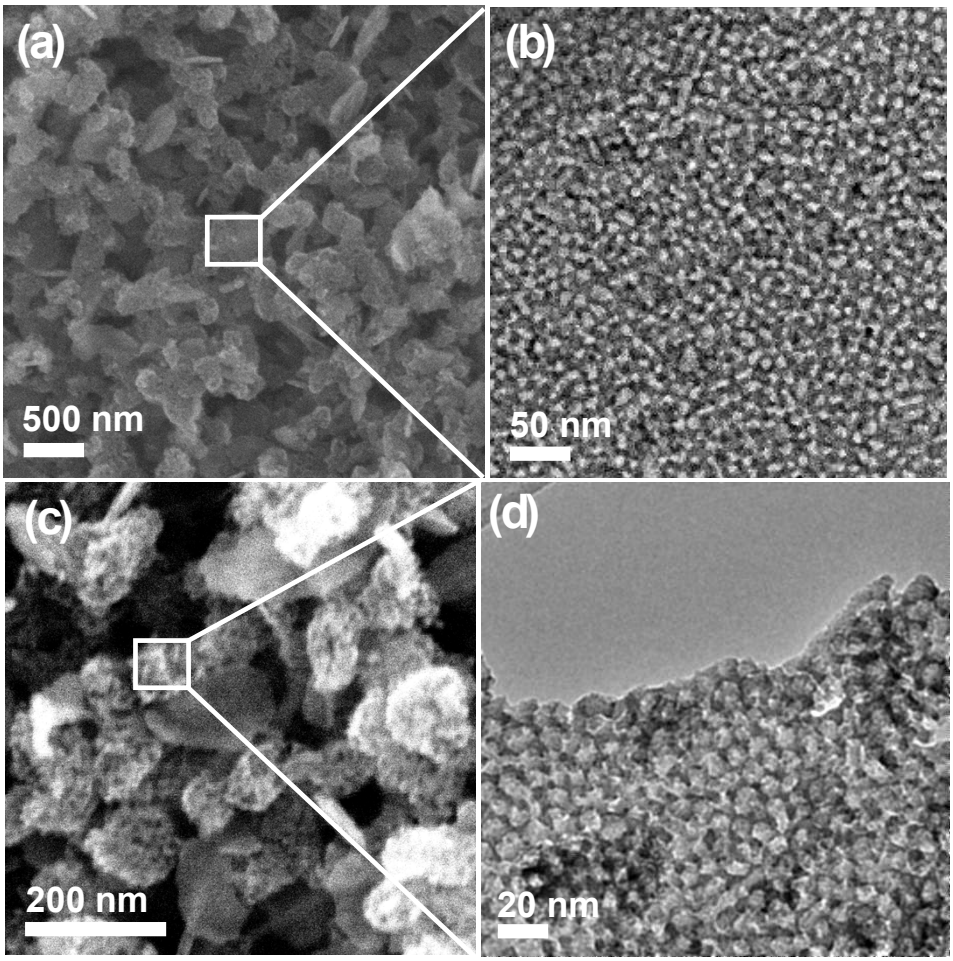

Fig. S1 (a, c) SEM and (b, d) TEM images of m-$MnCo_2O_4$.

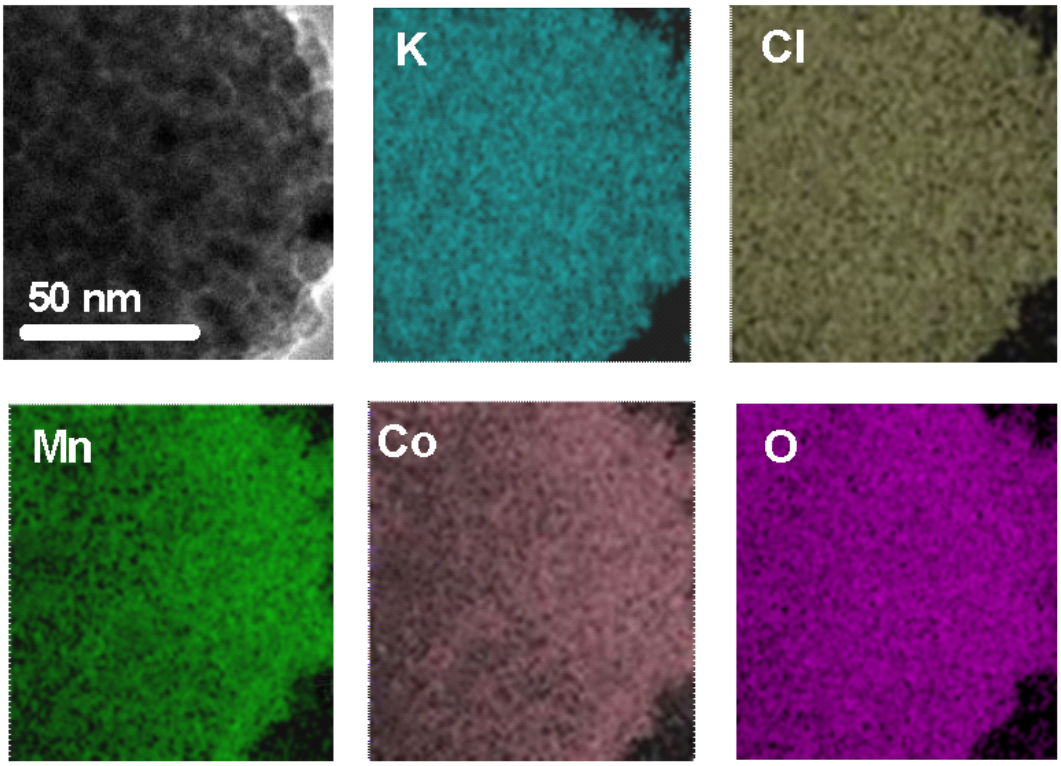

Fig. S2 EDS elemental mapping images of m-$MnCo_2O_4$+KCl before washing with water, showing a homogenous dispersion of KCl and $MnCo_2O_4$.

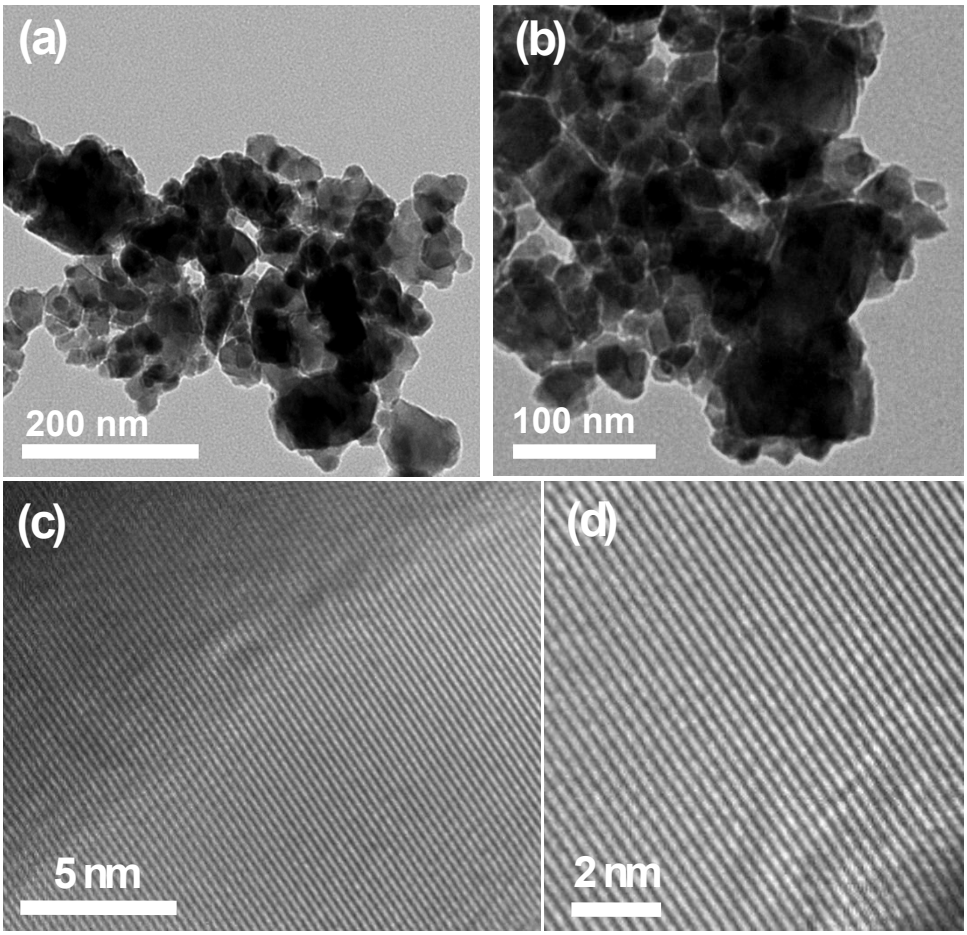

Fig. S3 (a, b) SEM and (c, d) TEM images of b-$MnCo_2O_4$ synthesized by the conventional sol-gel method.

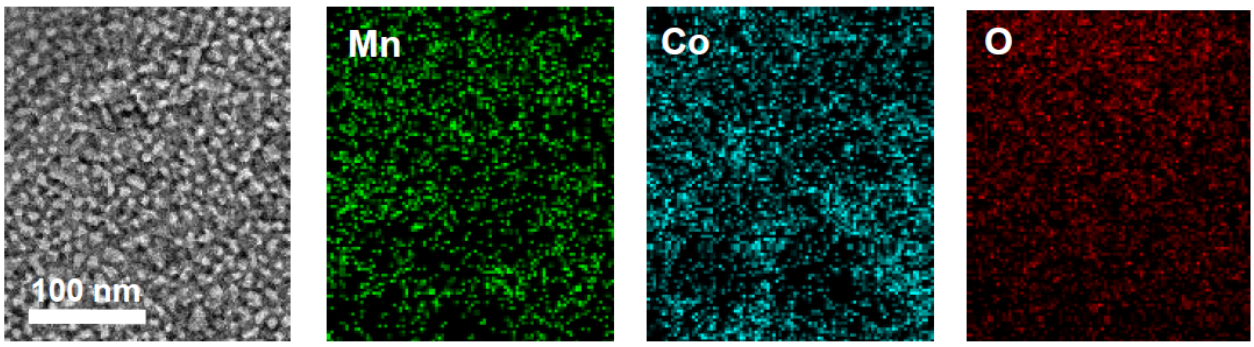

Fig. S4 EDS elemental mapping images of m-$MnCo_2O_4$ after washing with water, showing a homogenous dispersion of Mn, Co and O, without KCl species.

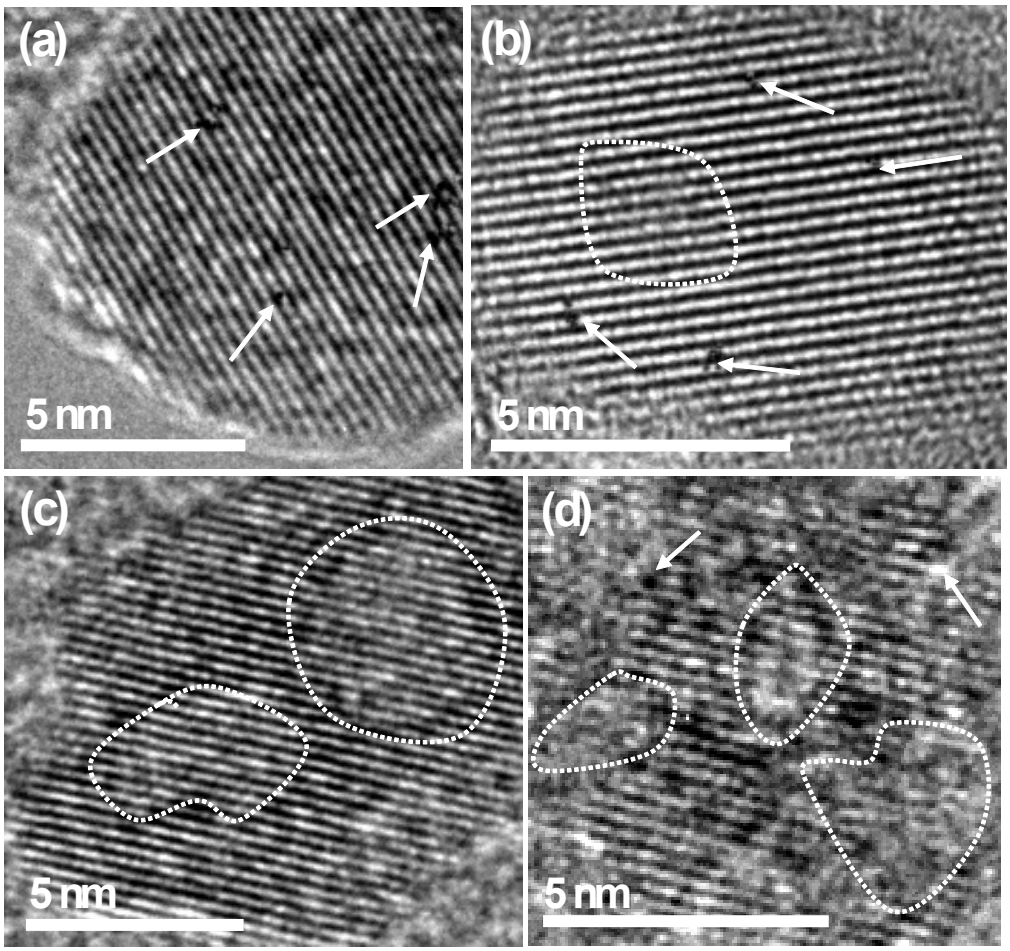

Fig. S5 HRTEM images of m-$MnCo_2O_4$, indicating the presence of abundant surface defects.

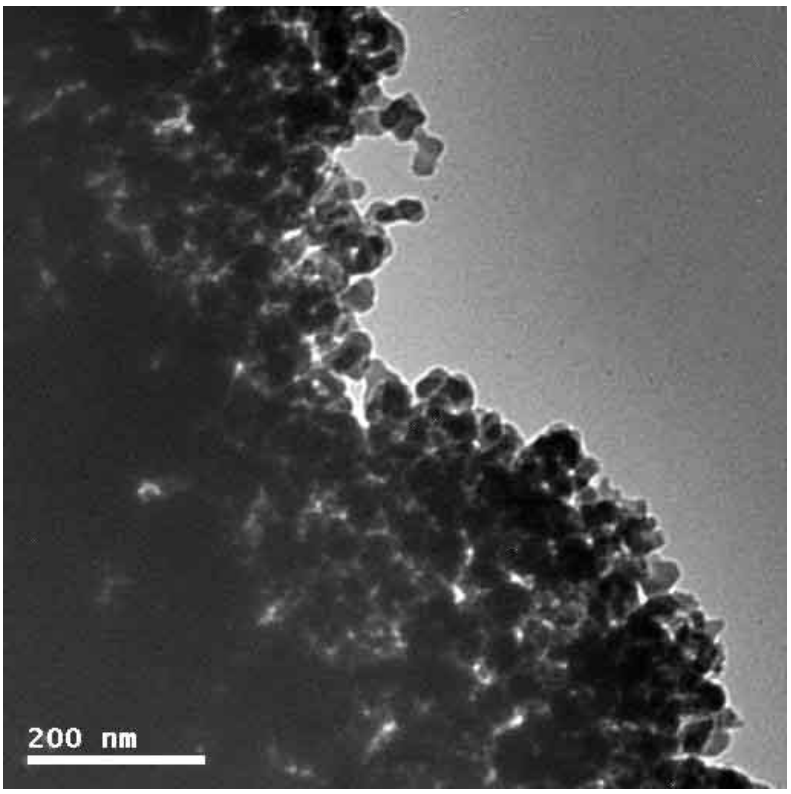

Fig. S6 TEM image of $MnCo_2O_4$ prepared in ethanol solution without extra water addition. During the synthesis of m-$MnCo_2O_4$, the solubility of the $MnCo_2O_4$ nanocrystals is much lower than that of KCl, The numerous fresh crystallites have abundant surface defects (isolated atoms, voids, steps, etc). Based on the heterogeneous nucleation mechanism, the closely succedent crystallization of KCl tends to happen in the uneven or defective zones of these crystallites with relatively high surface energy, which can efficiently reduce the surface energy and the crystallization energy barrier. However, if no extra water is added, too much KCl would crystallize from ethanol, which may aggregate together to form large KCl domains instead of homogenously assembly with $MnCo_2O_4$ nanocrystals. The $MnCo_2O_4$ sample prepared without extra water addition is shown in Fig. S8, in which no well-developed mesopores can be observed. Thus after multiple controlled experiments, a small amount of water of 290 μL is confirmed to be optimal for dissolving partial KCl and leaving the other as the template for mesopore construction in m-$MnCo_2O_4$.

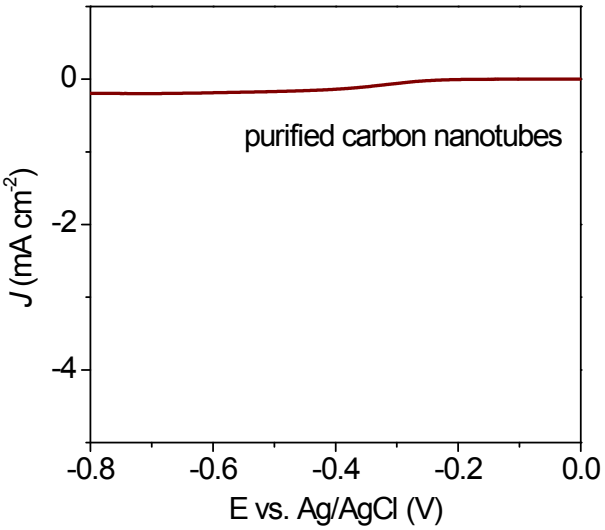

Fig. S7 The LSV of purified carbon nanotubes (1500 rpm, scan rate: 5 mV s^{-1}), indicating their negligible ORR activity.

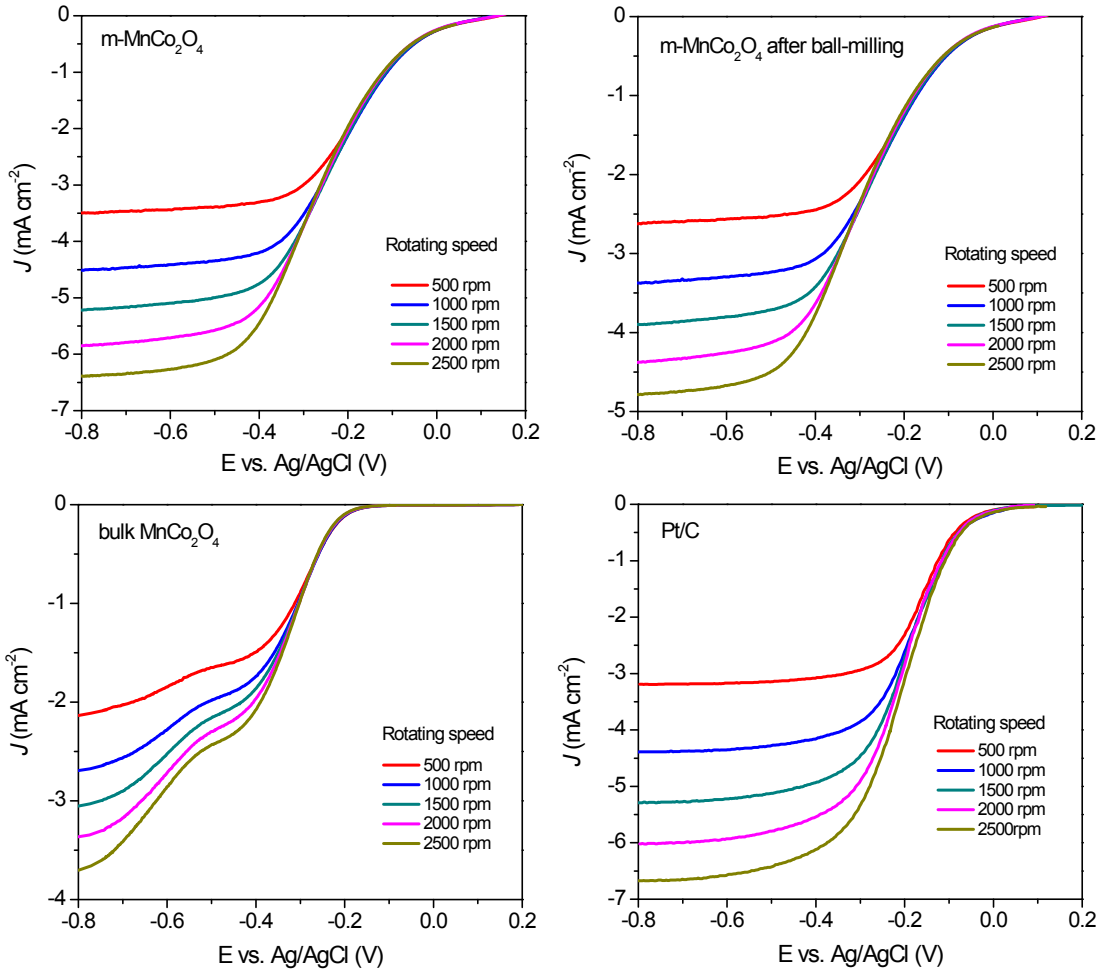

Fig. S8 LSVs of various electrocatalysts on RDE at different rotating rates (500 to 2500 rpm) in O_2-saturated 0.1 M KOH solution.

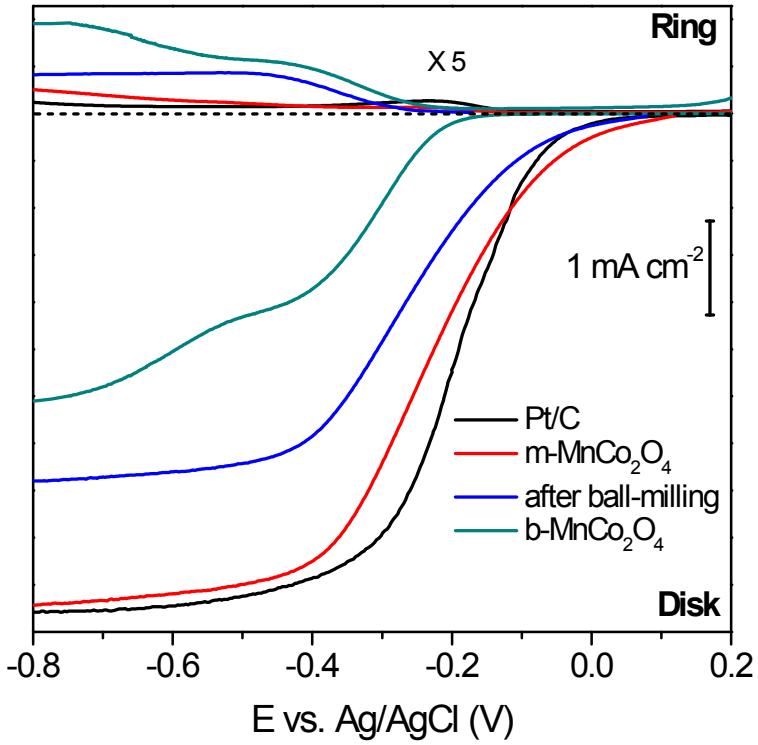

Fig. S9 Disk current densities (bottom) and the corresponding ring current densities (top) of various electrocatalysts on RRDE at a rotating rate of 1500 rpm in O_2-saturated 0.1 M KOH solution.

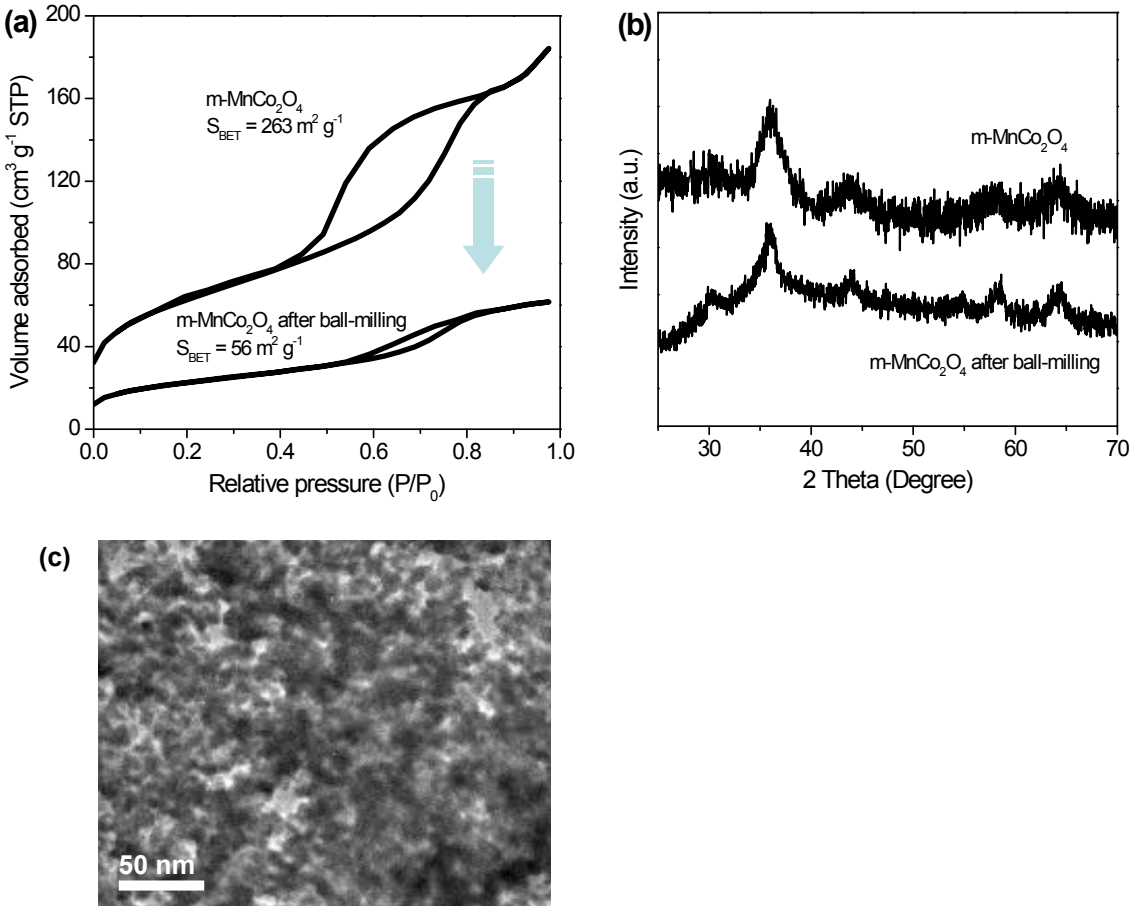

Fig. S10 (a) N_2 sorption isotherms and (b) wide-angle XRD patterns of m-$MnCo_2O_4$ before and after ball-milling. (c) TEM image of m-$MnCo_2O_4$ after ball-milling, showing the absence of well-developed mesopores.

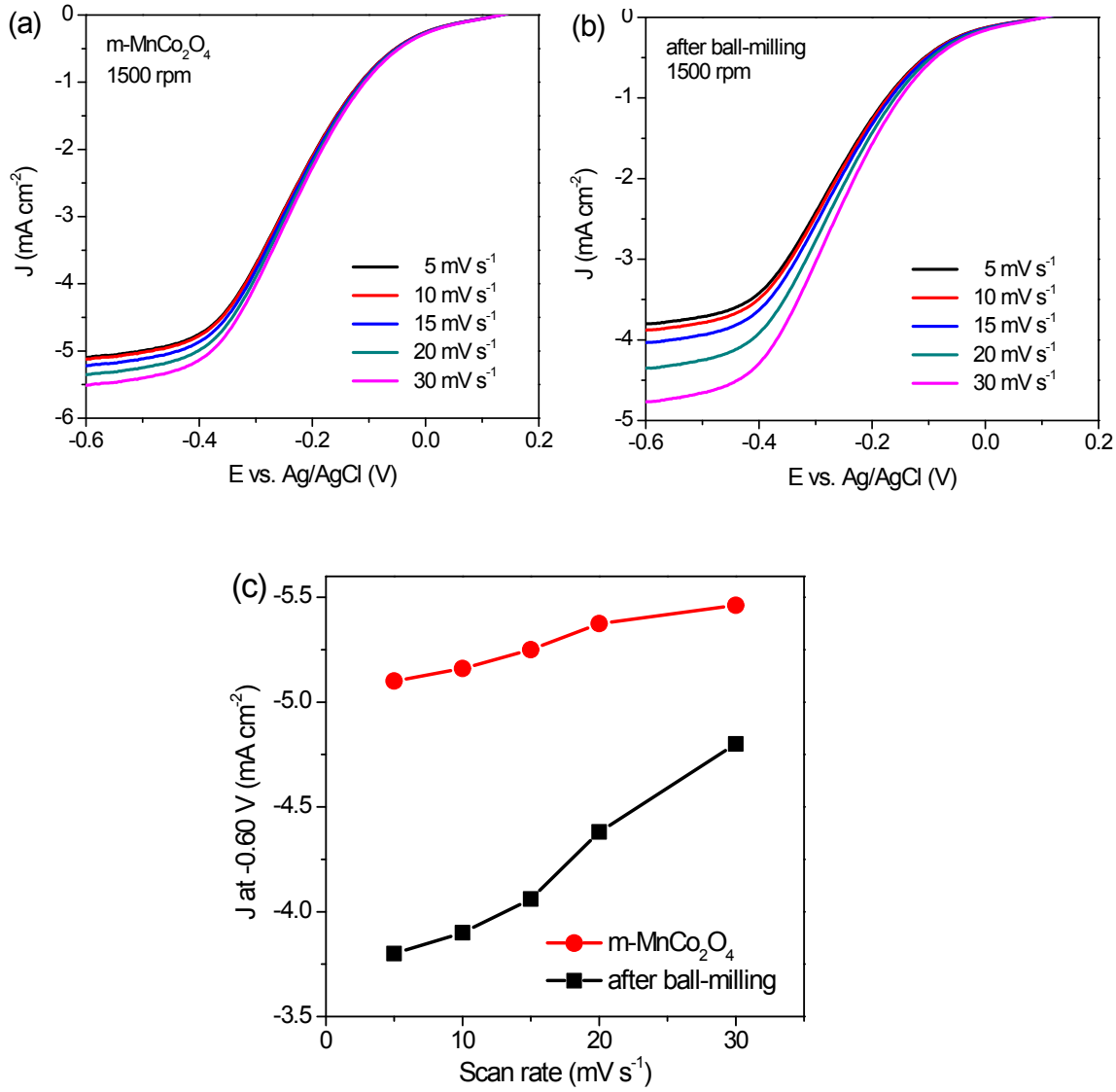

Fig. S11 LSVs recorded using a rotating rate of 1500 rpm at different scan rates for m-$MnCo_2O_4$ (a) before and (b) after ball-milling. (c) A comparison of the plots showing the current density at -0.6 V vs. scan rates for m-$MnCo_2O_4$ and b-$MnCo_2O_4$.

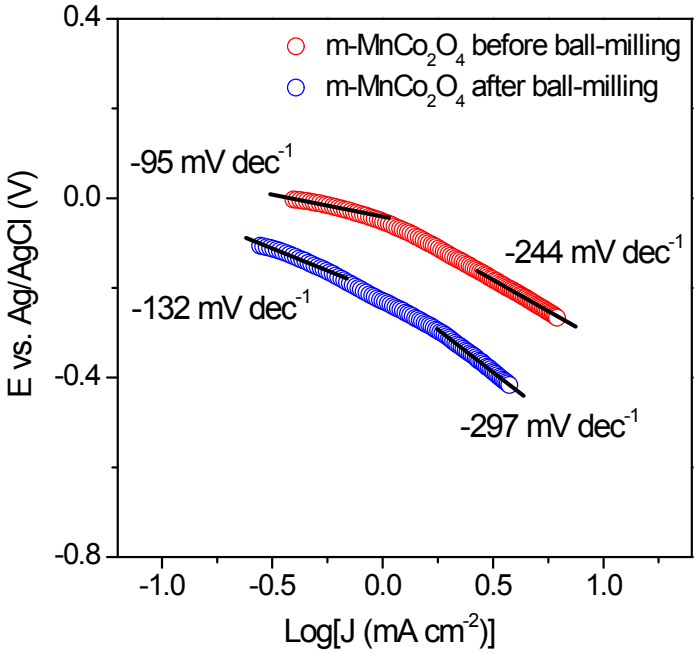

Fig. S12 Tafel plots for ORR on m-$MnCo_2O_4$ before and after ball-milling in O_2-saturated 0.1 M KOH. All data were recorded on RDE at 1500 rpm.

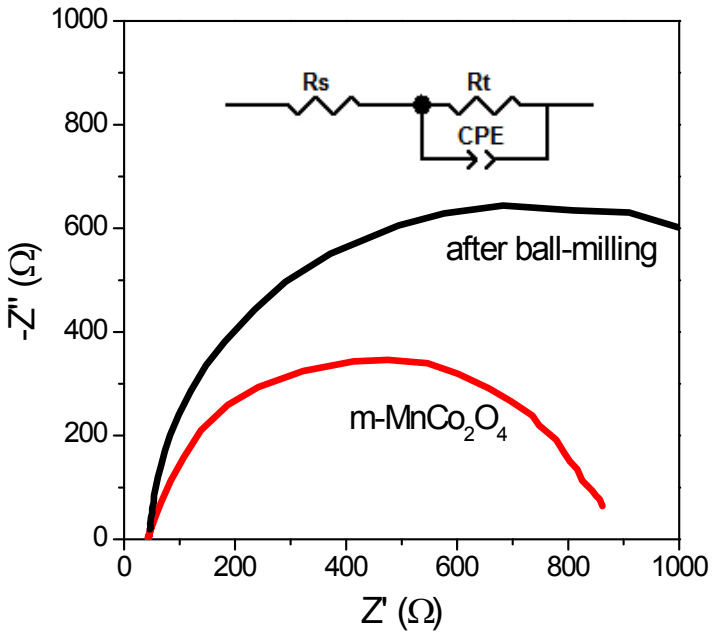

Fig. S13 (a) Electrochemical impedance spectrum (EIS) of m-$MnCo_2O_4$ before and after ball-milling (inset: the corresponding equivalent circuit diagram). The diameter of the semicircle for m-$MnCo_2O_4$ is much smaller than that of milled m-$MnCo_2O_4$ in the high-medium frequency region of the EIS due to a lower contact and charge transfer impedance for m-$MnCo_2O_4$.

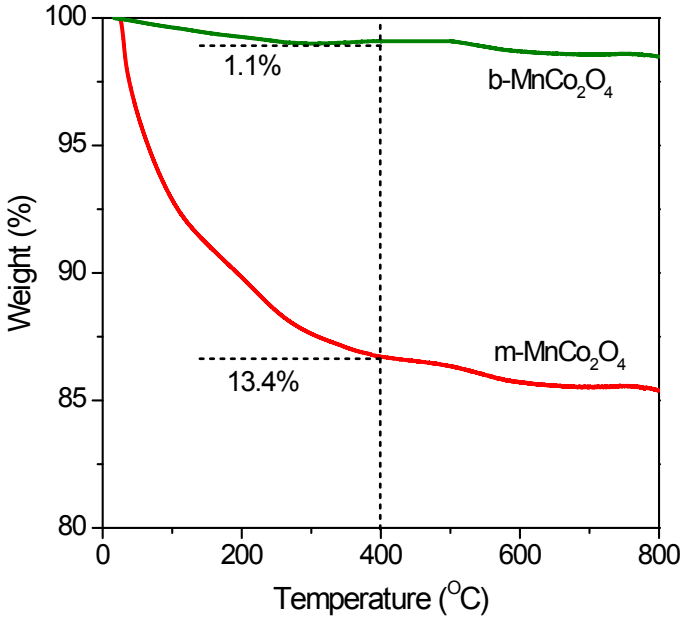

Fig. S14 TG measurements of m-$MnCo_2O_4$ and b-$MnCo_2O_4$. The weight loss from room temperature to 400 °C is due to the physi-/chemisorbed gases (e.g. O_2, CO_2) and H_2O, while the weight loss above 500 °C is attributed to the loss of lattice oxygens. The weight loss of m-$MnCo_2O_4$ (13.4%) is much higher than that of b-$MnCo_2O_4$ (1.1%) before 400 °C, which implies the larger amount of accessible adsorption sites in the framework of m-$MnCo_2O_4$, originated from the large amount of defects and high surface area.

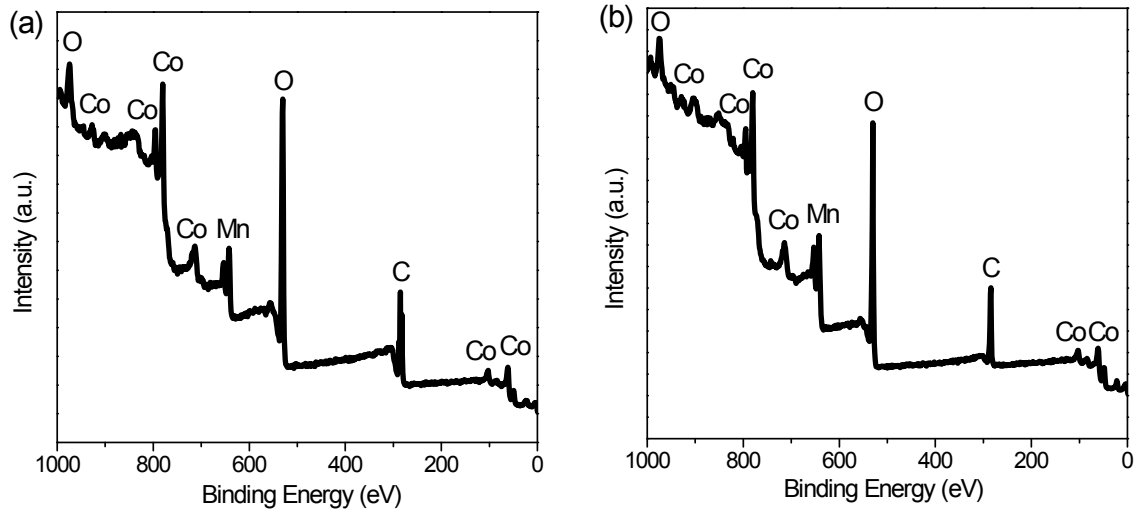

Fig. S15 The XPS survey spectra of (a) m-$MnCo_2O_4$ and (b) b-$MnCo_2O_4$.